Raman fingerprints of fractionalized Majorana excitations in the honeycomb iridate $Ag_3LiIr_2O_6$

Srishti Pal,[1] Vinod Kumar,[2] Debendra Prasad Panda,[3] A. Sundaresan,[3] Avinash V. Mahajan,[2] D. V. S. Muthu,[1] and A. K. Sood[1,*]

[1]*Department of Physics, Indian Institute of Science, Bengaluru 560012, India*

[2]*Department of Physics, Indian Institute of Technology Bombay, Mumbai 400076, India*

[3]*Chemistry and Physics of Materials Unit, Jawaharlal Nehru Center for Advanced Scientific Research, Jakkur P.O., Bengaluru 560064, India*

(Received 14 January 2022; revised 31 May 2022; accepted 6 June 2022; published 21 June 2022)

We report low-temperature (down to ∼5 K) Raman signatures of the recently discovered intercalated honeycomb magnet $Ag_3LiIr_2O_6$, a putative Kitaev quantum spin liquid (QSL) candidate. The Kitaev QSL is predicted to host Majorana fermions as its emergent elementary excitations through a thermal fractionalization of entangled spins $S = 1/2$. We observe evidence of this fractionalization in the low-energy magnetic continuum whose temperature evolution harbors signatures of the predicted Fermi statistics obeyed by the itinerant Majorana quasiparticles. The magnetic Raman susceptibility evinces a crossover from the conventional to a Kitaev paramagnetic state below the temperature of ∼80 K. Additionally, the development of the Fano asymmetry in the low-frequency phonon mode and the enhancement of integrated Raman susceptibilities below the crossover temperature signifies prominent coupling between the vibrational and Majorana fermionic excitations.

DOI: 10.1103/PhysRevB.105.235125

I. INTRODUCTION

The advent of quantum spin liquids (QSLs) has demonstrated the potential of condensed matter systems to host elusive low-energy excitations like Majorana fermions [1,2]. The Kitaev QSL with spins $S = 1/2$ on two-dimensional (2D) honeycomb lattice offers an ideal platform in this context due to the thermal fractionalization of the highly entangled spin excitations into pairs of noninteracting itinerant Majorana quasiparticles coupled to localized Z_2 gauge fluxes [3,4]. These two kinds of Majorana excitations, itinerant and localized, have well separated crossover temperature scales, the higher $T_h \sim 0.4$–$0.6J_K$ (J_K is the Kitaev coupling strength) related to the formation of matter Majorana fermions and the lower $T_l \sim 0.012$–$0.015J_K$ associated with condensation of localized flux [5,6].

The realization of Kitaev essence in real systems, as proposed in the pioneering works by Jackeli and Khaliullin [7] requires an intricate interplay of electronic (Coulomb) correlations, crystal-field effects, and spin-orbit entanglement as seen in certain heavy $4d$ and $5d$ transition metal compounds. Among these, the most noticeable ones are Na_2IrO_3 [8,9], α-$RuCl_3$ [10–12], α, β, and γ-Li_2IrO_3 [13,14]. Despite manifesting experimental signatures of fractionalization and hence showing proximity to Kitaev QSL state, all of these materials eventually exhibit long-range magnetic ordering at low temperatures [15]. This raises concern regarding the crucial role of non-Kitaev terms in the interaction Hamiltonian of the Kitaev systems affecting their pristine low-temperature QSL state.

Recently, a new set of Kitaev materials like $H_3LiIr_2O_6$ [16], Cu_2IrO_3 [17], and $Ag_3LiIr_2O_6$ have been synthesized from the parent compounds A_2IrO_3 (A = Na, Li) with the caveat that these compounds are susceptible to quenched disorders in their structure. In fact, the nature of disorder in these candidates becomes a key precursor in controlling the fate of their QSL ground state [18–21].

In this paper, we study the Raman scattering signatures of the recently synthesized [22] Kitaev QSL candidate $Ag_3LiIr_2O_6$. Derived from its precursor α-Li_2IrO_3 by replacing the interlayer Li atoms with silver retaining the honeycomb network of the $LiIr_2O_6$ (ab) planes, $Ag_3LiIr_2O_6$ crystallizes in the base centered monoclinic $C2/m$ structure. The LiO_6 octahedral connectivity linking the successive honeycomb planes in α-Li_2IrO_3 are replaced by perfectly linear (180°) O-Ag-O dumbbell bonds in $Ag_3LiIr_2O_6$, resulting in an ∼30% increase in the interlayer separation. The initial magnetic and thermodynamic studies on disordered $Ag_3LiIr_2O_6$ samples with extended Ag positional defects within the honeycomb layers, entrenched the validity of Kitaev QSL physics in this system by affirming the absence of any long-range magnetic order along with a two-step release of spin entropy at crossover temperatures $T_h \sim 75$ K and $T_l \sim 13$ K [23]. Later, a cleaner batch of samples exhibited a more pronounced and clear transition to long-range ordering below the Néel temperature $T_N \sim 10$ K while spin fluctuations remain present even in the ordered state down to 4.2 K [21,24,25]. Moreover, recent x-ray absorption and resonant inelastic x-ray scattering measurements on high-quality crystals confirmed the existence of a spin liquid ground state with moderate magnetic frustration [26].

Our measurements unveil the essence of fractionalization in $Ag_3LiIr_2O_6$ typified by the broad low-energy magnetic Raman continuum attributable to deconfined Majorana

*asood@iisc.ac.in

TABLE I. Rietveld refined parameters.

Space group	Lattice parameters	Refinement parameters	Atom	x	y	z	Occupancy
$C2/m$	$a = 5.2754(2)$ Å		Ir1	0.0000	0.3341(5)	0.0000	1
	$b = 9.1370(6)$ Å	$R_p = 20.3\%$	Li1	0.0000	0.0000	0.0000	1
	$c = 6.4827(4)$ Å	$R_{wp} = 17.6\%$	Ag1	0.0000	0.1725(7)	0.5	1
	$\alpha = 90°$	$R_{exp} = 7.03\%$	Ag2	0.0000	0.5	0.5	1
	$\beta = 105.73(1)°$	$\chi^2 = 6.25$	O1	0.0269(1)	0.0000	0.0198(1)	1
	$\gamma = 90°$		O2	0.4199(51)	0.3429(36)	0.1673(26)	1

quasiparticles obeying the predicted Fermi statistics. The presence of Majorana fermionic excitations in the system is further evidenced by their coupling with the low-frequency phonon mode causing development of clear Fano asymmetry in the line shape below the Majorana crossover temperature. Additionally, the Majorana-phonon coupling in the Kitaev paramagnetic phase is manifested through the departure of Raman intensity from the conventional thermal Bose contribution.

II. MATERIAL CHARACTERIZATION AND EXPERIMENTAL METHODS

High-quality polycrystalline samples of $Ag_3LiIr_2O_6$ were synthesized with the ion exchange method in two steps. In the first step the starting compound Li_2IrO_3 was prepared with a conventional solid state reaction method. The stoichiometric amounts of initial chemicals Li_2CO_3 (Alfa Aesar, 99.998%) and Ir-metal powder (Arro Biochem, 99.99%) was taken with 5% extra Li_2CO_3. The mixture was grounded well and heated at 650 °C for 15 h in open air with the heating rate of 40 °C/h. The mixture was again heated, with thorough grinding, at 950 °C and 1000 °C for 24 h each. In the next step, Li_2IrO_3 was mixed with $AgNO_3$ (Alpha Aesar, 99.998%) in a molar ratio of 1:3 and after mixing for 10 min this mixture was heated at 200 °C for 12 h with natural cooling. The final compound $Ag_3LiIr_2O_6$ was obtained after washing it multiple times with deionized water to remove the excess $AgNO_3$ and reaction product $LiNO_3$. The presence of nitrates was checked with KCl solution.

The powder x-ray diffraction measurements were performed with a PANalytical Empyrean diffractometer having a Cu target with $K\alpha$ radiation ($\lambda = 1.541\,82$ Å). The Rietveld refinement done using FULLPROF suite shown in Fig. 1(a) confirms phase purity with the monoclinic $C2/m$ crystallographic structure. We performed refinement without considering stacking fault by excluding the region 18°–21° (the Warren peak position). The extracted cell parameters and the atomic positions are given in Table I.

The magnetic susceptibility measurements were performed using a Magnetic Property Measurement System (MPMS-SQUID, Quantum Design, USA) in vibrating sample magnetometer mode under an applied field of 1 T. In zero-field-cooled (ZFC) measurement, the sample was first cooled to lowest temperature (2 K) without applying magnetic field and the measurements were carried out in a warming cycle. In field-cooled (FC) mode, the sample was cooled under the applied magnetic field and the magnetization was measured on warming. Figure 1(b) shows the temperature variation of the dc magnetic susceptibility between 2 and 300 K. The high temperature χ ($75 < T < 300$ K) is fitted well with the modified Curie-Weiss (CW) form $\chi = \chi_0 + C/(T - \Theta_{CW})$. The fit deviates below ~50 K along with a bifurcation between the

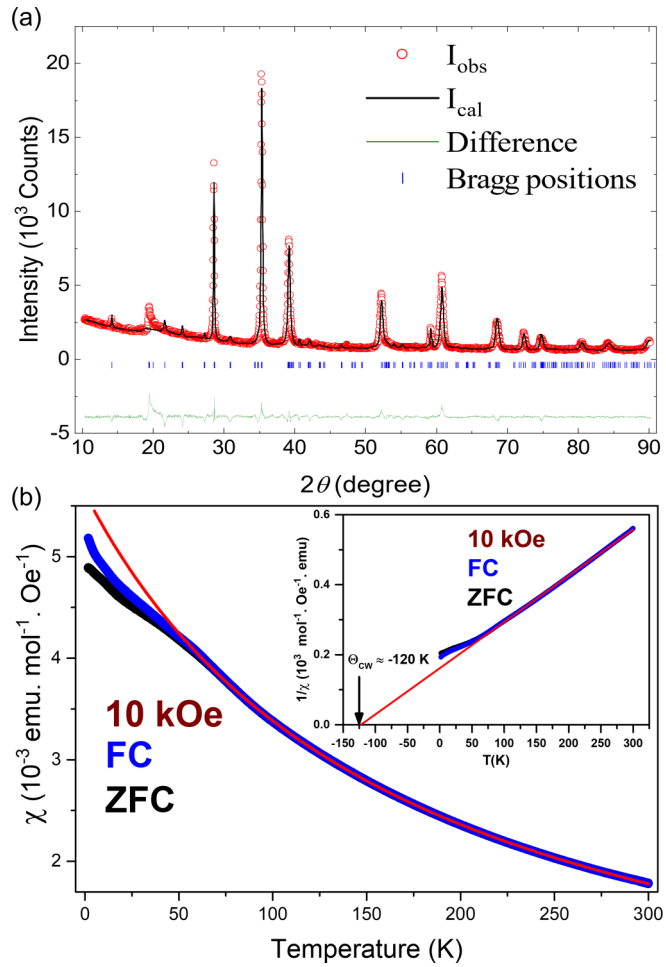

FIG. 1. (a) Rietveld refined powder x-ray diffraction pattern of $Ag_3LiIr_2O_6$. Experimental data and the calculated pattern are shown by red circles and black solid line, respectively. Reflection positions are indicated by blue vertical bars and the weighted difference between observed and calculated profiles is shown by the lower dark-green curve. (b) Temperature dependence of the dc magnetic susceptibility between 2 and 300 K at a field value of 1 T. Field-cooled (FC) and zero-field-cooled (ZFC) data are shown by blue and black circles, respectively. The red solid line is the Curie-Weiss (CW) fit. Inset shows the temperature variation of inverse susceptibility with the Curie-Weiss temperature extracted as 120 K.

ZFC and FC curves as reported earlier [25] to be originated from the quenched disorder of naturally occurring stacking faults present in the sample inducing localized moments. The inset of Fig. 1(b) shows the inverse dc susceptibility giving the Curie-Weiss temperature $\Theta_{CW} \approx -120$ K.

Unpolarized micro-Raman measurements were performed in backscattering geometry using a Horriba LabRAM HR Evolution Spectrometer equipped with a thermoelectric cooled charge coupled device detector (HORIBA Jobin Yvon, SYNCERITY 1024 × 256). The sample was excited using a 532-nm DPSS laser with ∼190 μW power falling on the sample. Temperature variation from 5 to 293 K with a temperature stability of $\approx \pm 1$ K was done with a closed cycle He cryostat (Cryostation S50, Montana Instruments).

III. RESULTS AND DISCUSSION

$Ag_3LiIr_2O_6$ crystallizes in monoclinic space group $C2/m$ (No. 12) with two formula units ($Z = 2$) per unit cell. Factor group analysis gives 15 Raman active Γ-point phonon modes as $\Gamma_{\text{Raman}} = 7A_g + 8B_g$ among which 11 modes could be detected at 5 K in our unpolarized Raman experiments denoted by M1–M11 in Fig. 2(a). The lowest frequency M1 mode unveils clear asymmetry in its line shape at low temperatures and hence is fitted with the asymmetric Breit-Wigner-Fano (BWF) profile [27] as shown in the inset of Fig. 2(a). The BWF function is defined as

$$I_{\text{BWF}}(\omega_s) = I_0 \frac{[1 + s/q]^2}{1 + s^2}, \tag{1}$$

where $s = (\omega_s - \omega_0)/w$. The parameters ω_s, ω_0, w, $1/q$, and I_0 are the Raman shift, the spectral peak center, the spectral width, the asymmetry factor, and the maximum intensity of the BWF line, respectively. The low-frequency region of the Raman profile is magnified and shown in Fig. 2(b) at a few selected temperatures. The phonon modes are superimposed on a weak low-energy continuum reminiscent of putative spin liquid materials [11–14,20] as being originated from the scattering of light by exotic Majorana fermionic excitations which are fractionalized in nature. Like the other derived QSL candidate Cu_2IrO_3 [20], $Ag_3LiIr_2O_6$ also lacks the peaking feature and the low-energy linear omega dependence of Raman intensity at low temperatures as was seen in the first-generation candidates [11,13,14] and hence masks the pristine low-frequency signatures of the Majorana fermions. This is owing to the intricate role of disorder present in these derived candidates which has been theoretically predicted to enhance the low-energy density of states of the Majorana fermionic excitations [28,29]. Equating the upper cutoff of ∼300 cm^{-1} of this broad Raman response to $3|J_K|$ (J_K is the Kitaev interaction strength), the theoretical estimate for the band edge of the Raman continuum from Majorana fermions [6], yields $|J_K| \approx 12$ meV which is in reasonable agreement with the Kitaev interaction strength obtained for this compound from recent density functional theory (DFT) calculations ($J_K \approx$ 11.4 meV) [25].

The smoking gun evidence for the emergence of the Kitaev QSL phase, as witnessed by all other Kitaev QSL materials [6,13,18,20], is the robust $(1 - f)^2$ scaling [where $f(\omega) = 1/(1 + e^{\hbar\omega/k_BT})$ is the Fermi distribution function]

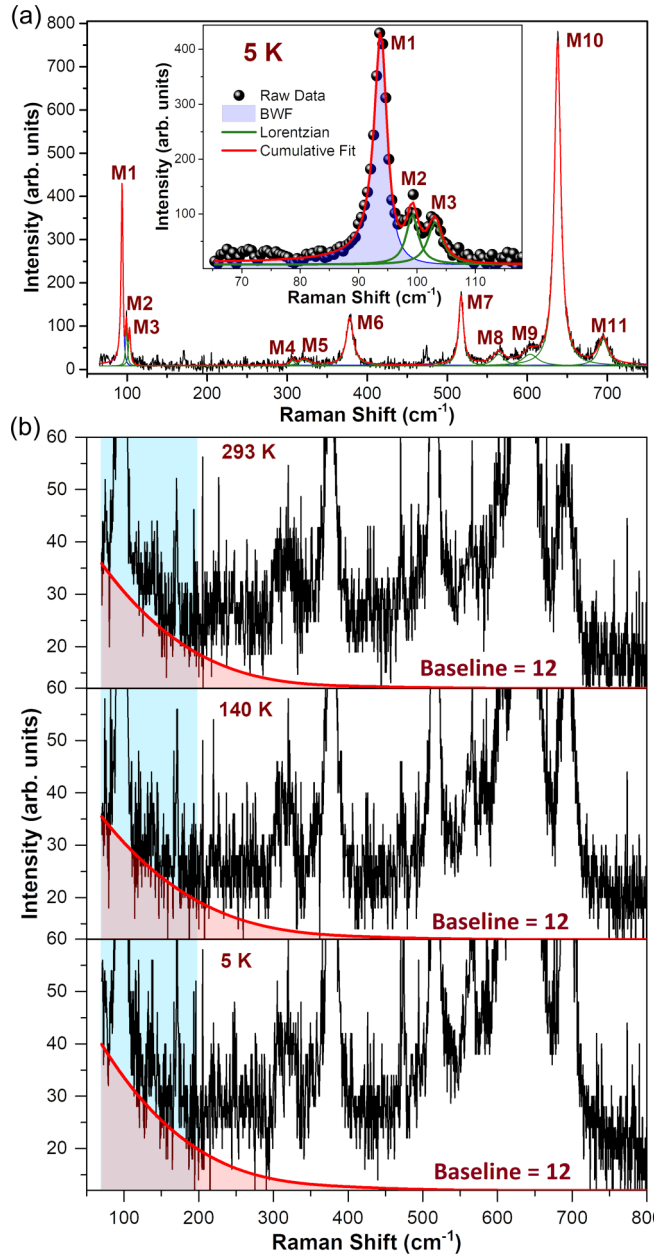

FIG. 2. (a) Raman spectra of $Ag_3LiIr_2O_6$ at 5 K in the spectral range 70–750 cm^{-1}. Black, blue, green, and red curves denote the raw data, phonon fits with Breit-Wigner-Fano (BWF) and Lorentzian line shapes, and the cumulative fit, respectively. Inset shows the asymmetry in the line shape of the M1 mode at 5 K fitted with the BWF function. (b) Magnified Raman profile at selected temperatures with the magnetic continuum shown by the red solid lines. The cyan shading indicates the frequency range of integration to extract I_{mid}.

of the integrated Raman continuum in the mid-frequency regime stemming from the creation of two itinerant Majorana fermions due to interaction with the probe photons. Figure 3(a) shows the temperature evolution of I_{mid} integrated in the frequency interval of 70–200 cm^{-1} [area under the red curves in the frequency interval shown by the cyan shading in Fig. 2(b)] chosen in accordance with the theoretical estimate given by Nasu *et al.* [6] (see Appendix B for robustness of the I_{mid} frequency window). The red curve in the inset

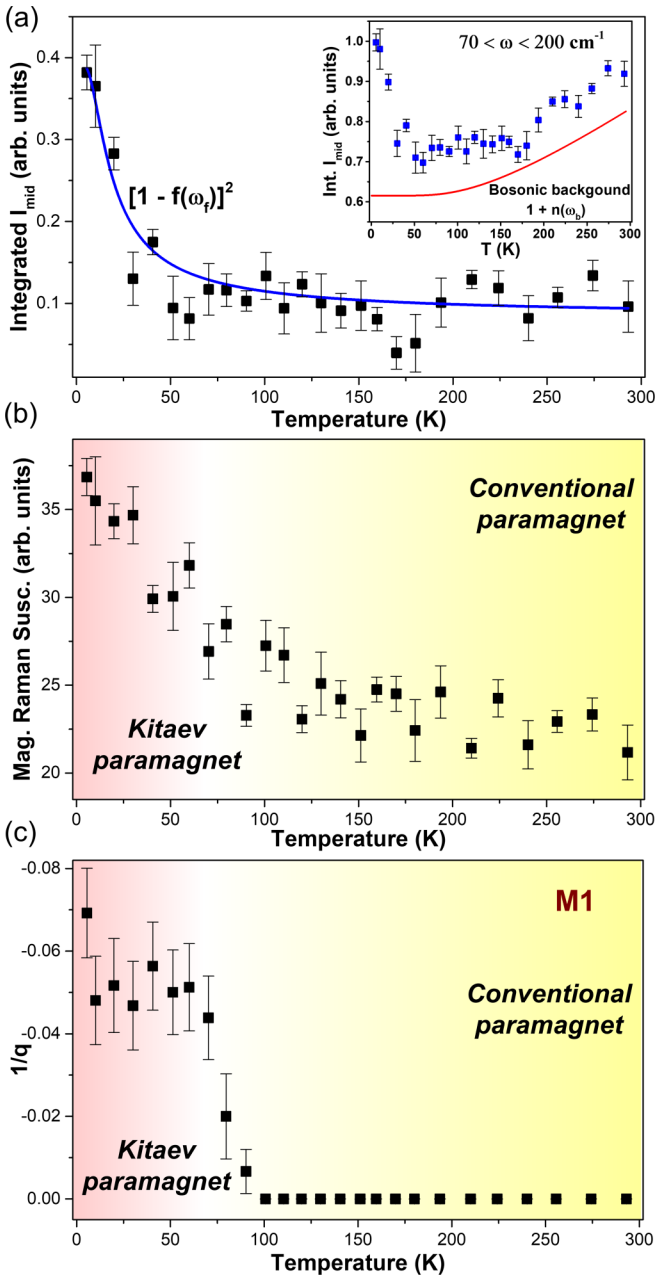

FIG. 3. (a) Integrated $I_{\rm mid}$ as a function of temperature in the frequency range 70–200 cm^{-1} after subtracting the bosonic background (shown in inset). The blue solid curve denotes fitting by the two-fermion scattering function $A + B(1-f)^2$ [$f = 1/(1+e^{\hbar\omega/k_BT})$ is the Fermi distribution function]. (b) Temperature evolution of magnetic Raman susceptibility calculations using the Kramers-Kronig relation. The shading marks the crossover between the conventional and Kitaev paramagnetic phases. (c) Temperature dependence of the asymmetry parameter $1/q$ of the M1 mode. The shading indicates the boundary between the conventional and Kitaev paramagnetic states.

denotes the bosonic background due to one particle scattering of the form $[1+n(\omega_b)] = 1/(1-e^{-\hbar\omega_b/k_BT})$, with $\omega_b =$ 35 meV, dominating the high-temperature regime. The main panel of Fig. 3(a) shows the temperature dependence of the magnetic contribution to integrated $I_{\rm mid}$ after subtracting the thermal Bose contribution. The blue curve represents the fitting of the magnetic continuum to the two-fermion scattering form $A + B[1 - f(\omega_f)]^2$, with $\omega_f = 2$ meV and reinforces the possibility of fractionalized Majorana fermionic excitations, corroborating $Ag_3LiIr_2O_6$ to be a potential spin liquid candidate.

Further exploration of the Majorana continuum requires extraction of the magnetic Raman susceptibility $\chi_R^{\rm dyn}$, a measure of the dynamic response from the spin system. Figure 3(b) exhibits the temperature dependence of $\chi_R^{\rm dyn}$ deduced by integrating the Raman conductivity $\frac{\chi''(\omega)}{\omega}$ from 70 to 400 cm^{-1} in accordance with the Kramers-Kronig relation [30,31],

$$\chi_R^{\rm dyn} = \lim_{\omega\to 0}\chi(k=0,\omega) \equiv \frac{2}{\pi}\int \frac{\chi''(\omega)}{\omega}d\omega. \qquad (2)$$

According to the fluctuation-dissipation theorem, the dynamical Raman tensor susceptibility $\chi''(\omega)$ is related to the Raman intensity $I(\omega)$ as

$$I(\omega) = 2\pi\int \langle R(t)R(0)\rangle e^{i\omega t}dt \propto [1+n(\omega)]\chi''(\omega), \qquad (3)$$

where $R(t)$ is the Raman operator which within the Kitaev QSL phenomenology, directly couples to the dispersing fractionalized Majorana fermions and hence, substantially projects the density of states (DOS) of weighted two-Majorana fermions. As seen from Fig. 3(b), $\chi_R^{\rm dyn}$ of $Ag_3LiIr_2O_6$ remains almost constant down to ~80 K below which it increases rapidly signifying moderate enhancement of the Majorana fermionic DOS driving the system to a Kitaev paramagnetic phase as also seen in other Kitaev QSL candidates α-$RuCl_3$ [12] and α-Li_2IrO_3 [14]. Also, the Majorana crossover temperature $T_h \sim 80$ K $\approx 0.6J_K$ as gleaned from the temperature evolution of $\chi_R^{\rm dyn}$ matches well with the theoretical predictions by Nasu *et al.* [5,6]. This value of T_h is in agreement with the earlier reported T_h of ~75 K by Bahrami *et al.* [21,23] from heat capacity measurements on the $Ag_3LiIr_2O_6$ system.

The temperature evolution of the $1/q$ asymmetry parameter for the M1 mode is shown in Fig. 3(c). The asymmetry parameter remains essentially zero down to the crossover temperature of $T_h \sim 80$ K below which it increases rapidly in magnitude with decreasing temperature. The emergence of this Fano resonance below T_h has its roots in the strong coupling between the discrete phonon mode (M1) and the magnetic continuum offered by the fractionalized Majorana excitations as has also been seen in other Kitaev QSL candidates [11,12,20]. All other phonon modes (M2–M11) are fitted with the symmetric Lorentzian line shape for the entire range of temperature. The phonon spectra do not reveal emergence of new modes or disappearance of existing modes, confirming the absence of any structural transition throughout the entire range of temperature.

Figures 4(a)–4(c) showcase the temperature evolution of the frequencies, linewidths, and the integrated susceptibilities of the strong phonon modes. The changes in frequencies and FWHMs, the real and imaginary parts of the phonon self-energy, of all the modes follow the typical monotonic lattice anharmonicity, as indicated by the simplified cubic anharmonic fits (red solid lines), arising from the decay of

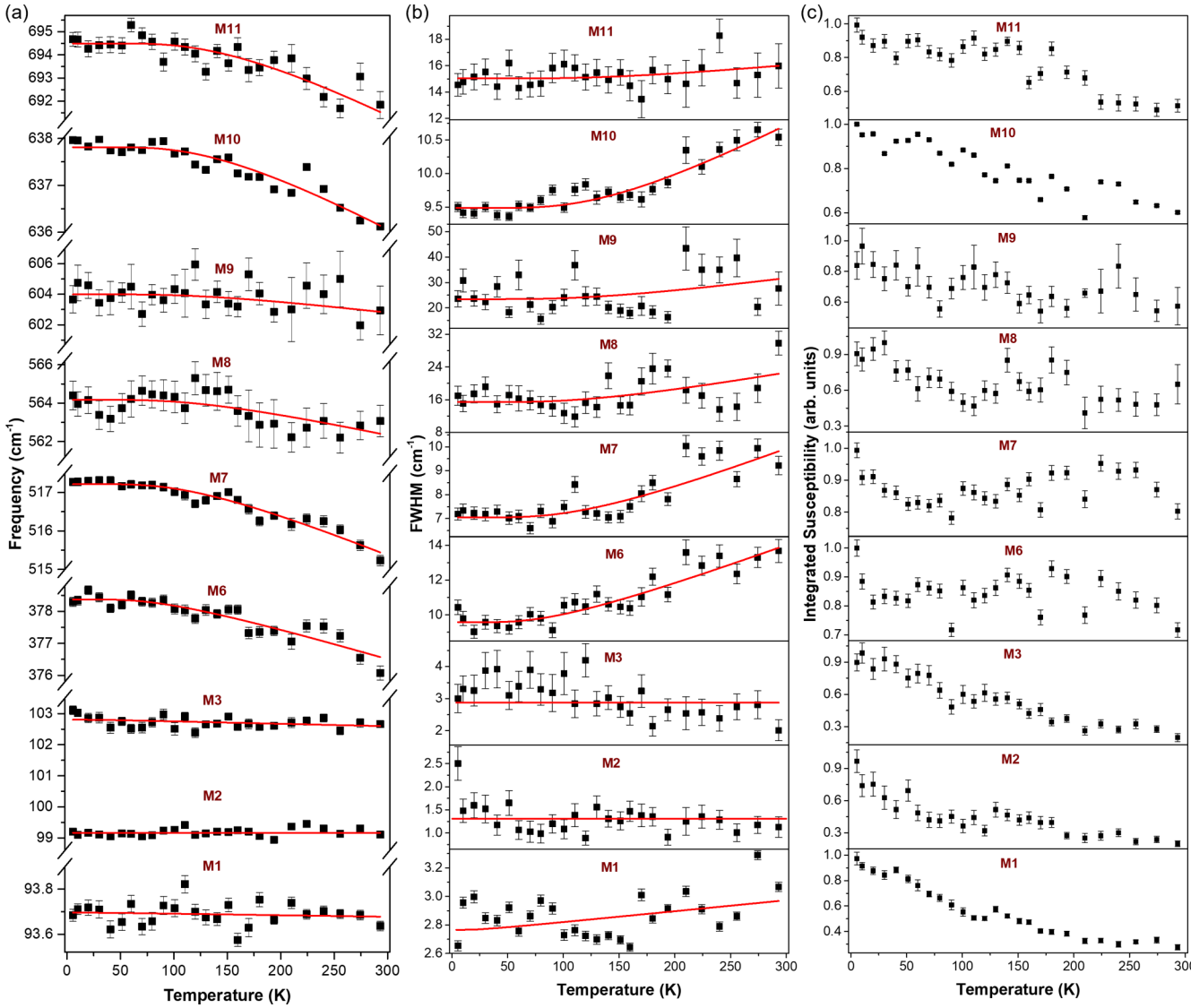

FIG. 4. Temperature evolution of (a) frequency, (b) FWHM, and (c) integrated susceptibilities of selected phonon modes. Red lines are the anharmonic fits to phonon frequencies and FWHMs. Blue lines are a guide to the eye indicating departures of the integrated susceptibilities below the Kitaev crossover temperature (shown by the shaded regions).

an optical phonon of frequency ω_0 into a phonon pair ($\omega_0/2$). See Appendix C for more details. All the phonon modes including the asymmetric Fano mode (M1) exhibit no noticeable anomaly in their temperature dependence of frequencies and linewidths as compared to the sister compound Cu_2IrO_3 [20]. However, the integrated susceptibilities of most of the phonon modes show anomalous rise with decreasing temperatures authenticating the development of spin-spin correlations in the Kitaev paramagnetic phase which affects the vibrational intensities through transfer of magnetic dipole intensity to the phonons due to significant coupling between the vibrational and fractionalized Majorana degrees of freedom [32].

IV. CONCLUSIONS

In summary, we have scrutinized the Raman scattering signatures of the proximate Kitaev QSL candidate $Ag_3LiIr_2O_6$. Similar to the sister compound Cu_2IrO_3, the broad low-energy magnetic continuum in $Ag_3LiIr_2O_6$ does not manifest the peaking feature and the low-energy linear omega dependence. This imposes further impetus to the role of quenched disorder in these derived Kitaev candidates, theoretically predicted to enhance the low-energy density of states of the Majorana fermionic excitations, as also discussed in Ref. [20]. The low-energy magnetic continuum, following the expected Fermi statistics in its temperature evolution, offers a Kitaev coupling strength of $J_K \approx 12$ meV, consistent with the value gleaned from the recent DFT calculations. The Kitaev coupling in this compound seems to be much weaker than that in Cu_2IrO_3 [20] as also indicated by recent DFT studies [25]. The Majorana crossover temperature of $T_h \sim 80$ K has been extracted from the development of dynamic spin susceptibility and is further supported by the emergence of a Fano asymmetric line shape for the lowest-frequency phonon mode. In contrast to Cu_2IrO_3, this material does not exhibit any noticeable anomaly in the temperature dependence of

phonon frequencies and linewidths, likely due to the suppressed Kitaev interaction strength and hence a much reduced phonon-Majorana coupling. However, in both the systems, the intensity of most of the Raman phonons show a prominent rise with decreasing temperatures due to the development of nearest-neighbor spin correlations in the system [20]. Our results thus provide the very first scattering signatures for the Kitaev spin liquid phase in the honeycomb iridate $Ag_3LiIr_2O_6$ and establish $Ag_3LiIr_2O_6$ as an ideal avenue to explore spin fractionalization and Majorana-phonon coupling.

ACKNOWLEDGMENTS

A.K.S. thanks Nanomission Council and the Year of Science professorship of DST for financial support. A.S. acknowledges International Centre for Materials Science, Jawaharlal Nehru Centre for Advanced Scientific Research, for providing their experimental facility. V.K. and A.V.M. acknowledge the central facilities provided by IIT Bombay and IRCC. A.V.M. acknowledges MHRD for funding of STARS research project ID 358.

APPENDIX A: DETAILS OF LOW-ENERGY CONTINUUM ANALYSIS

The scattering continuum arising from the Majorana excitation cannot be fitted to any specific form as indicated by all the earlier reports [6,12–14]. So, to avoid the contribution of the experimental noise, the low-energy background was taken as a smooth curve [shown by the red solid lines in Fig. 2(b); the area below these curves is shown by pink shaded regions and the area of integration for $I_{\rm mid}$ has been shown by the cyan shading] which has been subtracted from the raw data to fit the phonons. Hence, no phonon mode is included in the background calculation. The $I_{\rm mid}$ is first extracted in this procedure [shown by blue data points in the inset of Fig. 3(a)], and then the bosonic background [shown by the red solid curve in the inset of Fig. 3(a)] is fitted which is then subtracted from the $I_{\rm mid}$ to extract the fermionic contribution only and hence gives a reasonable fit [shown by the blue solid curve in Fig. 3(a)] to the two-fermion scattering form. This approach is similar to what was adopted by Nasu *et al.* earlier for the α-$RuCl_3$ system [6]. The errors in the integrated values were calculated from the standard deviation of the values extracted from several background curves obtained by slightly modifying the shape and the baseline (keeping well within the experimental noise) of the curve.

APPENDIX B: INTEGRATED $I_{\rm mid}$

Figure 5 shows the temperature evolution of integrated $I_{\rm mid}$ (normalized) in different energy windows. The typical scaling form of integrated $I_{\rm mid}$ remains robust under these moderate variations of the energy range.

APPENDIX C: LATTICE ANHARMONICITY

Temperature dependence of the phonon population is known as intrinsic anharmonic effect. Below the Debye temperature θ_D of the system, restricting to cubic (third-order)

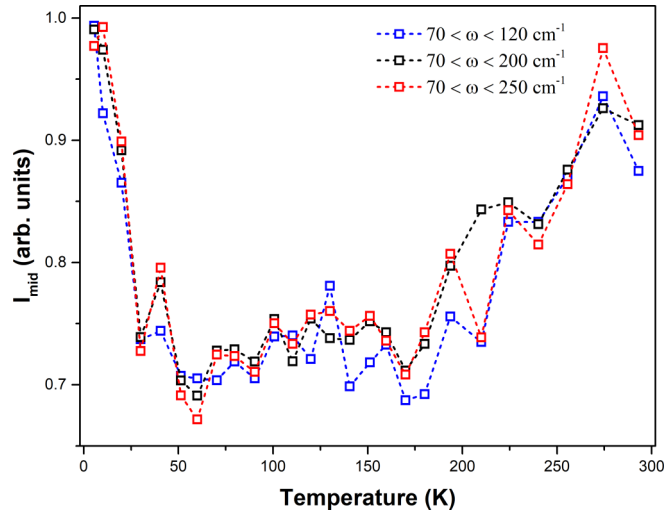

FIG. 5. Temperature dependence of integrated $I_{\rm mid}$ for different energy ranges.

corrections to phonon self-energy, the simplest decay channel is offered by each phonon of frequency ω_0 decaying into two phonons of equal energy, i.e., $\omega_1 = \omega_2 = \frac{\omega_0}{2}$. Under this cubic anharmonicity, the phonon frequency $\omega(T)$ and FWHM $\Gamma(T)$ can be given as [33]

$$\omega(T) = \omega_0 + A\Big[1 + 2n\Big(\frac{\omega_0}{2}, T\Big)\Big], \tag{C1}$$

$$\Gamma(T) = \Gamma_0 + B\Big[1 + 2n\Big(\frac{\omega_0}{2}, T\Big)\Big], \tag{C2}$$

where ω_0 and Γ_0 are constants at $T = 0$ K, $n(\frac{\omega_0}{2}, T)$ is the Bose-Einstein thermal population factor, and A (negative) and B (positive) are constants. In the fits shown in Figs. 4(a) and 4(b), ω_0 is extracted from the frequency fits and those values of ω_0 are used in the fitting of FWHMs. The fitting parameters ω_0, Γ_0, A, and B for different modes are given in Table II below.

TABLE II. List of fitting parameters for the cubic anharmonic fits to the phonon modes of $Ag_3LiIr_2O_6$.

Mode	ω_0 (cm^{-1})	A (cm^{-1})	Γ_0 (cm^{-1})	B (cm^{-1})
M1	93.7	0	2.7	0.03
M2	99.2	0	1.3	0
M3	102.8	−0.03	2.9	0
M6	379.7	−1.4	6.3	3.3
M7	519.5	−2.3	3.5	3.5
M8	566.8	−2.6	5	10.5
M9	605.9	−1.9	9.9	13.5
M10	641	−3.2	7.2	2.2
M11	701.3	−6.8	12.8	2.2

[1] Y. Kasahara, T. Ohnishi, Y. Mizukami, O. Tanaka, S. Ma, K. Sugii, N. Kurita, H. Tanaka, J. Nasu, Y. Motome, T. Shibauchi, and Y. Matsuda, Nature (London) **559**, 227 (2018).

[2] J. Alicea, Rep. Prog. Phys. **75**, 076501 (2012).

[3] A. Kitaev, Ann. Phys. **321**, 2 (2006).

[4] J. Knolle, D. L. Kovrizhin, J. T. Chalker, and R. Moessner, Phys. Rev. Lett. **112**, 207203 (2014).

[5] J. Nasu, M. Udagawa, and Y. Motome, Phys. Rev. B **92**, 115122 (2015).

[6] J. Nasu, J. Knolle, D. L. Kovrizhin, Y. Motome, and R. Moessner, Nat. Phys. **12**, 912 (2016).

[7] G. Jackeli and G. Khaliullin, Phys. Rev. Lett. **102**, 017205 (2009).

[8] K. Mehlawat, A. Thamizhavel, and Y. Singh, Phys. Rev. B **95**, 144406 (2017).

[9] S. H. Chun, J.-W. Kim, J. Kim, H. Zheng, C. C. Stoumpos, C. D. Malliakas, J. F. Mitchell, K. Mehlawat, Y. Singh, Y. Choi, T. Gog, A. Al-Zein, M. M. Sala, M. Krisch, J. Chaloupka, G. Jackeli, G. Khaliullin, and B. J. Kim, Nat. Phys. **11**, 462 (2015).

[10] S. H. Do, S. Y. Park, J. Yoshitake, J. Nasu, Y. Motome, Y. S. Kwon, D. T. Adroja, D. J. Voneshen, K. Kim, T. H. Jang, J. H. Park, K. Y. Choi, and S. Ji, Nat. Phys. **13**, 1079 (2017).

[11] L. J. Sandilands, Y. Tian, K. W. Plumb, Y. J. Kim, and K. S. Burch, Phys. Rev. Lett. **114**, 147201 (2015).

[12] A. Glamazda, P. Lemmens, S. H. Do, Y. S. Kwon, and K. Y. Choi, Phys. Rev. B **95**, 174429 (2017).

[13] A. Glamazda, P. Lemmens, S. H. Do, Y. S. Choi, and K. Y. Choi, Nat. Commun. **7**, 12286 (2016).

[14] G. Li, L.-L. Huang, X. Chen, C. Liu, S. Pei, X. Wang, S. Wang, Y. Zhao, D. Yu, L. Wang, F. Ye, J.-W. Mei, and M. Huang, Phys. Rev. B **101**, 174436 (2020).

[15] S. M. Winter, A. A. Tsirlin, M. Daghofer, J. van den Brink, Y. Singh, P. Gegenwart, and R. Valentí, J. Phys.: Condens. Matter **29**, 493002 (2017).

[16] K. Kitagawa, T. Takayama, Y. Matsumoto, A. Kato, R. Takano, Y. Kishimoto, S. Bette, R. Dinnebier, G. Jackeli, and H. Takagi, Nature (London) **554**, 341 (2018).

[17] M. Abramchuk, C. O. -Keskinbora, J. W. Krizan, K. R. Metz, D. C. Bell, and F. Tafti, J. Am. Chem. Soc. **139**, 15371 (2017).

[18] S. Pei, L. L. Huang, G. Li, X. Chen, B. Xi, X. W. Wang, Y. Shi, D. Yu, C. Liu, L. Wang, F. Ye, M. Huang, and J. W. Mei, Phys. Rev. B **101**, 201101(R) (2020).

[19] E. M. Kenney, C. U. Segre, W. Lafargue-Dit-Hauret, O. I. Lebedev, M. Abramchuk, A. Berlie, S. P. Cottrell, G. Simutis, F. Bahrami, N. E. Mordvinova, G. Fabbris, J. L. McChesney, D. Haskel, X. Rocquefelte, M. J. Graf, and F. Tafti, Phys. Rev. B **100**, 094418 (2019).

[20] S. Pal, A. Seth, P. Sakrikar, A. Ali, S. Bhattacharjee, D. V. S. Muthu, Y. Singh, and A. K. Sood, Phys. Rev. B **104**, 184420 (2021).

[21] F. Bahrami, E. M. Kenney, C. Wang, A. Berlie, O. I. Lebedev, M. J. Graf, and F. Tafti, Phys. Rev. B **103**, 094427 (2021).

[22] S. Bette, T. Takayama, V. Duppel, A. Poulain, H. Takagi, and R. E. Dinnebier, Dalton Trans. **48**, 9250 (2019).

[23] F. Bahrami, W. Lafargue-Dit-Hauret, O. I. Lebedev, R. Movshovich, H. Y. Yang, D. Broido, X. Rocquefelte, and F. Tafti, Phys. Rev. Lett. **123**, 237203 (2019).

[24] J. Wang, W. Yuan, T. Imai, P. M. Singer, F. Bahrami, and F. Tafti, Phys. Rev. B **103**, 214405 (2021).

[25] A. Chakraborty, V. Kumar, S. Bachhar, N. Büttgen, K. Yokoyama, P. K. Biswas, V. Siruguri, S. Pujari, I. Dasgupta, and A. V. Mahajan, Phys. Rev. B **104**, 115106 (2021).

[26] A.de la Torre, B. Zager, F. Bahrami, M. DiScala, J. R. Chamorro, M. H. Upton, G. Fabbris, D. Haskel, D. Casa, T. M. McQueen, F. Tafti, and K. W. Plumb, Phys. Rev. B **104**, L100416 (2021).

[27] E. H. Hasdeo, A. R. T. Nugraha, M. S. Dresselhaus, and R. Saito, Phys. Rev. B **90**, 245140 (2014).

[28] A. J. Willans, J. T. Chalker, and R. Moessner, Phys. Rev. Lett. **104**, 237203 (2010).

[29] A. J. Willans, J. T. Chalker, and R. Moessner, Phys. Rev. B **84**, 115146 (2011).

[30] J. S. Toll, Phys. Rev. **104**, 1760 (1956).

[31] C. Sun and N. A. Sinitsyn, J. Phys. A: Math. Theor. **48**, 505202 (2015).

[32] S. J. Allen and H. J. Guggenheim, Phys. Rev. Lett. **21**, 1807 (1968).

[33] P. G. Klemens, Phys. Rev. B **148**, 845 (1966).